EXPERIMENTAL AND NUMERICAL INVESTIGATION OF THE TOUGHENING MECHANISMS IN BIOINSPIRED COMPOSITES PREPARED BY FREEZE CASTING

Jingyu Liu[a], Ruixiang Bai[b], Zhenkun Lei[b], Chun Xu[c], Qingsong Ye[c], Wayde Martens[a], Prasad KDV Yarlagadda[a], Cheng Yan[a,*]

[a]School of Chemistry, Physics and Mechanical Engineering, Science and Engineering Faculty, Queensland University of Technology (QUT), Brisbane, Queensland, Australia.

[b]State Key Laboratory of Structural Analysis for Industrial Equipment, International Center for Computational Mechanic, Dalian University of Technology, Dalian, China.

[c]School of Dentistry, University of Queensland (UQ), Brisbane, Queensland, Australia.

*Corresponding author. Email address: c2.yan@qut.edu.au

Abstract

Strength and toughness have been generally deemed as two incompatible properties in many materials. However, balanced toughness and strength have been observed in biomaterials, whose hard and soft phases are arranged into unique and hierarchical architectures. Therefore, it is necessary to understand the underpinning toughening mechanisms and develop reliable procedures that can mimic these unique structures at different length scales. Here, alumina-Poly(methyl methacrylate) (PMMA) composites were prepared using freeze casting combined with interface modification (silanization treatment). High failure strain (~4.5%) is achieved in these composites. The overall toughness can be tailored through modifying the interfacial strength between alumina and PMMA. A weaker interface (~8MPa) leads to a greater toughness (3.1 MPa $m^{1/2}$), which is even greater than the constituent phases, i.e., alumina (2.71 MPa $m^{1/2}$) and PMMA (1.1

MPa $m^{1/2}$). Using a cohesive zone model and extended finite element method (XFEM), the toughening mechanism has been investigated.

Keywords

A. Bioinspired composites; B. Fracture toughness; B. Interfacial strength; C. Modelling; C. Finite element analysis (FEA)

1. Introduction

Ceramics can have superb stiffness and yield strength while maintaining lightweight[1]. However, the intrinsic brittle nature of ceramics, largely due to strong covalent and ionic bonds, often leads to brittle failure under mechanical loads. Development of damage-resistant ceramics is thus in pressing needs. Fortunately, lessons can always be obtained from nature[2, 3]. Biological materials possess desirable energy-absorbing behaviour, attributed to their unique structural characteristics[4]. For example, nacre is a highly damage-tolerant material and attracting increasing research effort[5, 6]. With 95 vol.% of layered aragonite ($CaCO_3$) platelets (hard phase) and 5 vol.% of nacre protein (soft phase) in the structure, nacre can absorb a high level of energy during fracture, i.e., 350~1240 J/m^2, about 3000 times higher than pure aragonite[7]. The underpinning mechanism is considered to be crack delocalization and interfacial hardening via platelet interlocking.

Through mimicking the graded structures observed in natural composites at different length scales, advances have been achieved in the development of bioinspired ceramics[8-10]. For example, ceramic-polymer type composites were fabricated to replicate the structural features of nacre via different processes, including biomimetic mineralization[11], additive manufacturing[12, 13], self-assembly[14, 15], and slip casting[16]. Recently, freeze casting has been proven to be a promising alternative[17,

18]. Specifically, the freeze casted samples with spontaneous anisotropy are considered to be beneficial for heat management [19] and thermal stability [20] and therefore are in high demand in electronics industry.

The toughening mechanisms in these composites were often interpreted as plastic deformation of the soft phase and crack deflection and bridging. As well known, interfacial strength plays an important role in stress transfer and energy dissipation in composites[21]. To date, however, there have been relatively few attempts to evaluate the interfacial property between the hard and soft phases, and its effect on toughening mechanism in these bioinspired composites[22-24].

In this work, with combined freeze casting and surface modification process, we successfully produced nacre-like composites with high toughness and strength. The interface strength and overall mechanical behaviour were investigated using bend tests. Extended finite element method (XFEM) and cohesive zone model were used to simulate the crack initiation and propagation. These results further confirm that interfacial strength is the key factor governing the overall mechanical performance of nacre-like composites.

2. Materials and methods

2.1 Freeze casting

Freeze casting is a shape forming technique employing ice as the structural template, as shown in Figure 1. In this work, all samples were prepared using a custom-designed freeze casting equipment. The slurry was prepared by dispersing 20 vol.% alumina nanoparticles (200nm, Sigma Aldrich) in 80 vol.% of deionized water. Then 1 wt.% of poly(ethylene glycol) (PEG, Mn10000, Sigma Aldrich) and 1 wt.% of poly(e-ethyl-2-oxazoline) (PEOX, 50,000, Sigma Aldrich) were added to the mixture as lubricant and binder, respectively. Darvan 811 (R.T. Vanderbilt Company) was added as dispersing

agent with a varying load from 1 wt.% to 8 wt.%. The mixed slurry was magnetically stirred for 12 hours, followed by degassing under low vacuum for 15 min to fully remove the air bubbles. All samples were frozen at a constant rate (moving velocity of ice surface) of 3.175 mm/min, which led to a lamellar structure with uniformly dispersed pores. The samples were kept at -10 °C for 24h to release the internal stress. Then, the samples were mechanically removed from the mould by punching and sublimated in a freeze dryer (Vertis Sentry 5L) at 310Pa for 24 hours to remove the ice. Finally, the samples were sintered at 1550 °C for 4 hours.

To introduce PMMA into the lamellar structures, the samples were chemically etched using Piranha solution (1:1 H_2O_2:30 vol.% H_2SO_4) for 10 minutes, and rinsed in ultrapure water and dried at room temperature for 24 hours. Diluted grafting agent 3-(trimethoxysilyl)propyl methacrylate (γ-MPS, Sigma Aldrich, 1:1 acetone: γ-MPS by volume) was used as coupling agent to create covalent bonding between alumina and PMMA via condensation reaction. Then, the samples were immersed into methyl methacrylate (MMA, Sigma Aldrich) monomers initiated by Benzoyl peroxide (BPO, 0.1 wt.% AIBN in MMA) at 50 °C for 24h. Finally, the composite samples were thermally treated at 100 °C for 1 h to fully complete the polymerization reaction. Hereafter, the composite samples produced with different grating time (0~48 hours) are referred as G0, G3, G6, G12, G24 and G48, respectively.

2.2 Characterisation

Flexural strength (σ) and toughness (K_{Ic}) were evaluated using bend tests based on ASTM C1161 and ASTM 1820 (Instron), respectively. For flexural toughness testing, firstly, the specimens were carefully cut off by water jet and grinding to the size with a width W~2.5 mm, a thickness B~2 mm and a length L~15 mm. Then, these samples were

notched using a rotational diamond saw from the bottom, and the notch root was further sharpened by sliding razor blade with diamond slurries (particle size 0.2 μm). The depth of the notches is about ~50% of the width (W). The testing was carried out by a displacement control at the loading rate 0.001mm/s with a support span of 10 mm.

Similarly, beam samples (with a width W~2mm and a thickness B~1.5mm) were prepared for flexural strength test. The tests were performed at a crosshead rate of $1.0*10^{-4}$ mm/mm/s. Three samples were tested for each group.

To understand the effect of interfacial strength between alumina and PMMA on the overall mechanical behaviour of the composites, specially designed bend samples were prepared, as shown in Figure 2. More details are provided in supplementary materials. The interface is located in the centre of bulk alumina and PMMA. In this way, the maximum normal stress corresponding to the failure point during bending can be regarded as the stress required to separate the interface, i.e., the interfacial strength. The dimensions of the sample are 2.5mm (width, *b*), 2.5mm (height *h*), and 20mm (span, L) and tests were performed at a constant load rate at $5*10^{-4}$ mm/mm/s. The interfacial strength can be evaluated using

$$\sigma = \frac{3PL}{2bh^2} \quad (1)$$

where P is the external load. The loading rate in interfacial strength tests was 0.5 μm/s.

Fourier Transform infrared spectroscopy (FTIR) spectrums of silane treated samples were obtained by Bruker Optics system, which helps to quantitatively analyse the content of γ-MPS molecules attached on the Alumina surface. The microstructure of samples was analysed by field emission scanning electron microscope (FE-SEM, Tescan).

2.3 Numerical simulation

It is still a technical challenge to predict crack initiation and propagation if the crack path is not defined. In this work, we use cohesive zone method (CZM)[25] to describe the interfaces between the hard and soft phases, which is implemented in an extended simulated finite element (XFEM) code[26]. The advantage is the random growth of a crack can be simulated. In the CZM model, the actual failure stress measured from the interfacial strength test (Figure 3) is used as failure criterion to simulate the crack initiation. As shown in Figure 2, the numerical model contains polymer phase which is randomly dispersed in the ceramic matrix. The polymer phase is in elliptical shape with the long axis of 15~ 30 μm. The selection of size and distribution of the polymer phase is referred to the porosity observed in the samples after freeze casting. The details of the simulation parameters are summarized in Supplementary files.

3. Results and discussion

3.1 Microstructures of the composites

Figure S2 shows the cross section and longitudinal section of the alumina/PMMA composites prepared by 1 wt%, 4 wt% and 8 wt% of dispersants. Lamella structures are observed in all samples. The average pore spacing and wall thickness for sample prepared with 4 wt% dispersant are 12μm and 7μm respectively. It is clear that the microstructure is affected by the dispersant loading. Although dispersant helps to improve the homogeneity, it may introduce some hole defects at a high loading. The compressive tests results (Figure S3) further confirms that the suitable selection of dispersants improve the mechanical performance for alumina matrix as the samples with 4 wt% dispersants have highest compressive strength (37.6 MPa).

3.2 Interfacial strength

As shown in Figure 2(a), a type of sample is designed to evaluate the interface strength between alumina and PMMA. The alumina surface was treated using silane to modify the interfacial strength. The FTIR spectrum is shown in Figure 3(a). G0 is pure alumina without any treatment, which has a nearly smooth spectrum from 1100 cm^{-1} to 1800 cm^{-1}. For the treated samples, the absorption bands around 1720 cm^{-1} and 1637 cm^{-1} are attributed to enhanced vibrations in the C=O and C=C groups, respectively. The bands at 1320 cm^{-1} and 1299 cm^{-1} are associated with C-O-C bonds and CH_3 groups. The band close to 1168 is from the increased vibrations in Si-O-C bonds. The intensity of the vibration generally increases with the treatment time. After 12 hours, the difference between each FTIR spectrum is hard to distinguish, thus we assume that the adsorption and desorption of γ-MPS molecule attained a balance.

As shown in Figure S4, the interfacial strength is supposed to come from two factors: one is the chemical bond between alumina and PMMA; the other one is the transgranular fracture of PMMA material. The stress-strain curves from the interfacial strength test are shown in Figure 3(b). It is clear that silanization treatment significantly affects the interfacial strength. For example, the strength increases from 3.14MPa to 12.44MPa after 24 h treatment (G24). After 6 h treatment, the increase of strength is limited but increased elastic modulus is observed up to 24 h. Further increase of treatment time (48 h) does not lead to a further increase of elastic modulus. It is noticeable that there is a small drop of interfacial strength in the sample G48. As shown in Figure S4, alumina surface in sample G48 has lower roughness compared with G12 and G24. We speculate that the decrease of interfacial strength in sample G48 can be partially explained by simple mechanical interlocking phenomenon between the surface microroughness and the surrounding

PMMA phase. Less anchoring point on the smooth surface of G48 resulting in the drop of interfacial strength compared with other rough samples.

To understand the energy dissipation during the interface separation, the interfacial energy was evaluated from the stress-strain curves, as shown in Figure 3(c). The interfacial energy has a peak value corresponding to 6 h silane treatment. After that, the absorbed energy gradually decreases as the binding becomes stronger but brittle.

3.3 Fracture mechanisms

Figure 4(a) shows the stress-strain curves of the freeze casted samples, evaluated by the three-point bend test. The flexural strength is in the range of 20.2~ 72.2 MPa. It is clear that the flexural strength and Young's modulus increases with the grafting time during the sample preparation, due to increased binding strength. The elastic strain increases from 0.025 to 0.51 with grating time up to 24 hours. On the other hand, little plastic deformation can be observed in the samples with short grafting time (<6 hours). As shown in Figure 4(b), alumina has higher strength but extremely lower failure strain up to 0.07%[27-29] whereas PMMA has a totally opposite mechanical property with strength of 16 MPa and failure strain of 4.4%[30]. From our results, the flexural strength of alumina/PMMA composites is higher than the calculation by the 'rule of mixtures' of pure alumina and PMMA.

Fracture toughness K_{Ic} is also evaluated using the bend test with notched samples. As shown in Figure 4(c), the K_{Ic} for the sample after 3 h grafting (G3) is 3.1 MPa $m^{1/2}$, which is higher than alumina (K_{Ic} =2.71 MPa $m^{1/2}$) and PMMA (K_{Ic} =1.1 MPa $m^{1/2}$)[14, 31, 32]. It is worth noting that K_{Ic} doesn't increases linearly with the grafting time. Sample G3 has an intermediate (balanced) interface strength, flexural strength, elastic strain, which

contribute to the highest fracture toughness. The results of interface and flexural tests are summarized in supplementary file Table S1.

The stress field around the notch and crack growth were investigated using the finite element method. The cohesive model was used to simulate the interface failure between the polymer and alumina phases, with the measured interfacial strength (3~13 MPa). For simplicity, three representative interface strengths, i.e., 5MPa, 10MPa and 15MPa were adopted. As shown in supplementary file Figure S6, high von Mises stress is observed in front of the notch, the interface between two phases and the loading points. The magnified images show interface failure between the polymer and alumina, corresponding to the stress magnitude and locations shown in Figure S6(a-c). As shown in Figure S6(a), significant interface damage is observed in the sample with low interface strength (5MPa).

Figure 5(a) shows the force-displacement curves of the simulation models with different interfacial strengths. It can be seen from the initial elastic deformation part (from 0 to ~0.6μm) that higher binding strength yields high stiffness for the whole system. Moreover, it is clear that the stiffness and max failure load increase with the interfacial strength. The work and strain energy can be estimated by the area under the curves. The dissipated energy including the energy consumed during deformation, friction, fracture and contact, as shown in Figure 5(b), can be used to indicate the toughness. It is clear that the sample of intermediate interfacial strength (10 MPa) has the highest toughness, which coincides with the results obtained from the flexural bending test.

To understand the failure mechanism, the crack propagation path was examined and compared with the simulations. Figure 6(b) shows the propagation path in the sample of low interfacial strength (5 MPa). The main crack penetrates into the polymer phase, followed by interface delamination between the two phases. With the increase of the

interface strength to 10 MPa, interface delamination does not happen after the main crack goes into the polymer phase. Instead, a secondary crack initiates from the other side of the soft phase, followed by coalescence with the main crack. In addition, crack deflection and branching take place, leading to a higher level of energy dissipation. This is consistent with the experimental observation in the sample G3 with an interfacial strength of 8.26 MPa. From Figure 6(e) and Figure S5(a), it can be seen that several crack deflections form along the main crack. As further checking with the magnified image (Figure 6(f)), it is found that the main crack tends to follow the weak interface between alumina and PMMA, thus bypass the polymer phase. However, if the aspect ratio of PMMA phase is too large, the crack will directly across the PMMA granule. In addition, It is noticeable that some large particles bridging the two separated pieces of the specimen even after it heavily damaged, as shown in Figure S5(b) and Figure S5(c). This crack bridging phenomenon is another toughen mechanism that these bioinspired composites possess.

There is a high degree of similarity of the crack route between sample of interfacial strength 10 MPa and 15 MPa, as shown in Figure 6(c) and (d). In the sample with interfacial strength of 15 MPa, the crack also forms at the head of the notch and propagates straight within the alumina until it touches the first interface. Then it experiences a small deflection when passing through the interface, and temporarily stopping inside of the polymer phase. After that, a secondary crack forms ahead of the polymer phase. Both the main crack and secondary crack keep developing when the displacement load are giving the specimen. The main crack will stop at the second interface, which splits the polymer part into two halves in the end. Thereafter, failure behaviour concentrates at the secondary crack.

As inspired by nacre, which is a natural structural material, our composites have a lot of common features in internal structure: both of them comprise hard and soft phases arranged in hierarchical architectures. Noticeably, as nacre has a soft matrix (protein) and hard filler (aragonite), our bioinspired composites have a different layout, whose matrix is hard (alumina) and particles are soft (PMMA). This structural layout helps to improve the crack resistance while maintaining enough stiffness of the composite. The toughening mechanisms of nacre and our composites are very similar: crack deflection and crack branching are considered to be the main toughen mechanisms for them; interfaces between hard phases and soft phases play an important role in controlling the overall mechanical behaviour[33-35].

4. Conclusion

Together with silanization surface treatment, directional freeze casting is used to prepare alumina/PMMA bioinspired composites. High fracture toughness (over 3.1 MPa $m^{1/2}$) and failure strain (over 4.5%) have been achieved, which are better than alumina (2.4 MPa $m^{1/2}$ and 4.4%) and PMMA (1.1 MPa $m^{1/2}$ and 0.07%). The failure mechanism is investigated using combined cohesive zone model and extended finite element method (XFEM). It has been found that the overall mechanical behaviour of the composites can be tailored via modifying the alumina/PMMA interfacial strength. A relatively weak interface may improve the overall fracture toughness, attributed to crack deflection and branching. We believe these outcomes point out a way to create new bioinspired materials with balance mechanical behaviour, and provide a better understanding of the toughening mechanisms in nacre-like composites.

Acknowledgement

The authors wish to acknowledge the Central Analytical Research Facility (CARF) at Queensland University of Technology (QUT). Jingyu Liu acknowledges the financial support from the China Scholarship Council and a Top-Up scholarship from Queensland University of Technology. The financial support from an ARC Discovery Project (DP180101955) is greatly appreciated.

References

[1] M.F. Ashby, D. Cebon, Materials selection in mechanical design, Le Journal de Physique IV 03(C7) (1993) C7-1-C7-9.

[2] U.G. Wegst, H. Bai, E. Saiz, A.P. Tomsia, R.O. Ritchie, Bioinspired structural materials, Nat Mater 14(1) (2015) 23-36.

[3] C. Huang, Q. Cheng, Learning from nacre: Constructing polymer nanocomposites, Composites Science and Technology 150 (2017) 141-166.

[4] M. Yang, N. Zhao, Y. Cui, W. Gao, Q. Zhao, C. Gao, H. Bai, T. Xie, Biomimetic Architectured Graphene Aerogel with Exceptional Strength and Resilience, ACS Nano 11(7) (2017) 6817-6824.

[5] B. Ji, H. Gao, Mechanical Principles of Biological Nanocomposites, Annual Review of Materials Research 40(1) (2010) 77-100.

[6] M.A. Meyers, P.-Y. Chen, A.Y.-M. Lin, Y. Seki, Biological materials: Structure and mechanical properties, Progress in Materials Science 53(1) (2008) 1-206.

[7] The mechanical design of nacre, Proceedings of the Royal Society of London. Series B. Biological Sciences 234(1277) (1988) 415-440.

[8] J.W. Dunlop, P. Fratzl, Bioinspired composites: Making a tooth mimic, Nat Mater 14(11) (2015) 1082-3.

[9] J.A. Faber, A.F. Arrieta, A.R. Studart, Bioinspired spring origami, Science 359(6382) (2018) 1386-1391.

[10] M. Schaffner, J.A. Faber, L. Pianegonda, P.A. Ruhs, F. Coulter, A.R. Studart, 3D printing of robotic soft actuators with programmable bioinspired architectures, Nat Commun 9(1) (2018) 878.

[11] L.-B. Mao, H.-L. Gao, H.-B. Yao, L. Liu, H. Cölfen, G. Liu, S.-M. Chen, S.-K. Li, Y.-X. Yan, Y.-Y. Liu, S.-H. Yu, Synthetic nacre by predesigned matrix-directed mineralization, Science (2016).

[12] W. Zhang, F. Zhang, X. Lan, J. Leng, A.S. Wu, T.M. Bryson, C. Cotton, B. Gu, B. Sun, T.-W. Chou, Shape memory behavior and recovery force of 4D printed textile functional composites, Composites Science and Technology 160 (2018) 224-230.

[13] J.J. Martin, B.E. Fiore, R.M. Erb, Designing bioinspired composite reinforcement architectures via 3D magnetic printing, Nat Commun 6 (2015) 8641.

[14] H.L. Gao, S.M. Chen, L.B. Mao, Z.Q. Song, H.B. Yao, H. Colfen, X.S. Luo, F. Zhang, Z. Pan, Y.F. Meng, Y. Ni, S.H. Yu, Mass production of bulk artificial nacre with excellent mechanical properties, Nat Commun 8(1) (2017) 287.

[15] P. Das, H. Thomas, M. Moeller, A. Walther, Large-scale, thick, self-assembled, nacre-mimetic brick-walls as fire barrier coatings on textiles, Sci Rep 7 (2017) 39910.

[16] H. Le Ferrand, F. Bouville, T.P. Niebel, A.R. Studart, Magnetically assisted slip casting of bioinspired heterogeneous composites, Nat Mater 14(11) (2015) 1172-9.

[17] S. Deville, The lure of ice-templating: Recent trends and opportunities for porous materials, Scripta Materialia (2017).

[18] X. Zhao, A. Lai, C.A. Schuh, Shape memory zirconia foams through ice templating, Scripta Materialia 135 (2017) 50-53.

[19] J. Han, G. Du, W. Gao, H. Bai, An Anisotropically High Thermal Conductive Boron Nitride/Epoxy Composite Based on Nacre‐Mimetic 3D Network, Advanced Functional Materials 29(13) (2019).

[20] G. Du, A. Mao, J. Yu, J. Hou, N. Zhao, J. Han, Q. Zhao, W. Gao, T. Xie, H. Bai, Nacre-mimetic composite with intrinsic self-healing and shape-programming capability, Nat Commun 10(1) (2019) 800.

[21] M. Shahidi, B. Pichler, C. Hellmich, How interface size, density, and viscosity affect creep and relaxation functions of matrix-interface composites: a micromechanical study, Acta Mechanica 227(1) (2015) 229-252.

[22] B. Lé, N. Moës, G. Legrain, Coupling damage and cohesive zone models with the Thick Level Set approach to fracture, Engineering Fracture Mechanics 193 (2018) 214-247.

[23] G.X. Gu, F. Libonati, S.D. Wettermark, M.J. Buehler, Printing nature: Unraveling the role of nacre's mineral bridges, J Mech Behav Biomed Mater (2017).

[24] B. Ji, H. Gao, Mechanical properties of nanostructure of biological materials, Journal of the Mechanics and Physics of Solids 52(9) (2004) 1963-1990.

[25] D. Wang, W. Xu, S. Chen, M. Zang, An extrinsic cohesive shell model for dynamic fracture analyses, Theoretical and Applied Fracture Mechanics 97 (2018) 165-176.

[26] T. Belytschko, Elastic crack growth in finite elements with minimal remeshing, International Journal for Numerical Methods in Engineering 45(5) (1999) 601-620.

[27] W.D. Callister, Materials science and engineering : an introduction, 9th edition. ed., Wiley, Hoboken, NJ, 2014.

[28] W.D. Callister, D.G. Rethwisch, Materials science and engineering: an introduction, John Wiley & Sons New York2007.

[29] W.D. Callister, Materials science and engineering: an introduction.

[30] M. Hashem, M.F. Rez, H. Fouad, T. Elsarnagawy, M. Elsharawy, A. Umar, M. Assery, S.G. Ansari, Influence of Titanium Oxide Nanoparticles on the Physical and Thermomechanical Behavior of Poly Methyl Methacrylate (PMMA): A Denture Base Resin, Science of Advanced Materials 9(6) (2017) 938-944.

[31] S.R. Choi, J.A. Salem, Fracture toughness of PMMA as measured with indentation cracks, Journal of Materials Research 8(12) (2011) 3210-3217.

[32] E. Munch, M.E. Launey, D.H. Alsem, E. Saiz, A.P. Tomsia, R.O. Ritchie, Tough, Bio-Inspired Hybrid Materials, Science 322(5907) (2008) 1516-1520.

[33] A. Khayer Dastjerdi, R. Rabiei, F. Barthelat, The weak interfaces within tough natural composites: experiments on three types of nacre, J Mech Behav Biomed Mater 19 (2013) 50-60.

[34] Z.-H. Xu, X. Li, Deformation Strengthening of Biopolymer in Nacre, Advanced Functional Materials 21(20) (2011) 3883-3888.

[35] J. Kim, C. Baillie, J. Poh, Y.-W. Mai, Fracture toughness of CFRP with modified epoxy resin matrices, Composites Science and Technology 43(3) (1992) 283-297.

Figure Captions

Figure 1 Schematic of sample preparation

Figure 2 a) Specimen for interfacial strength test; b) Set-up for interfacial strength test; c) Numerical simulation model for bioinspired material

Figure 3 a) FTIR of samples G0-G48 (treated for 0~48 hours); b) Interfacial stress-strain curves; c) interfacial energy

Figure 4 Results of bend test: a) stress-strain curves; b) flexural strength and elastic strain; c) fracture toughness

Figure 5 a) load-displacement curve from simulation; b) damage work dissipation-displacement curve from simulation

Figure 6 a) randomly distributed particle model for numerical simulation; b)-d) damage pattern for composites with different interfacial strength from 5 MPa to 15 MPa: b) interfacial strength of 5 MPa; c) interfacial strength of 10 MPa; d) interfacial strength of 15 MPa; e) crack path of G3; f) magnified image of e

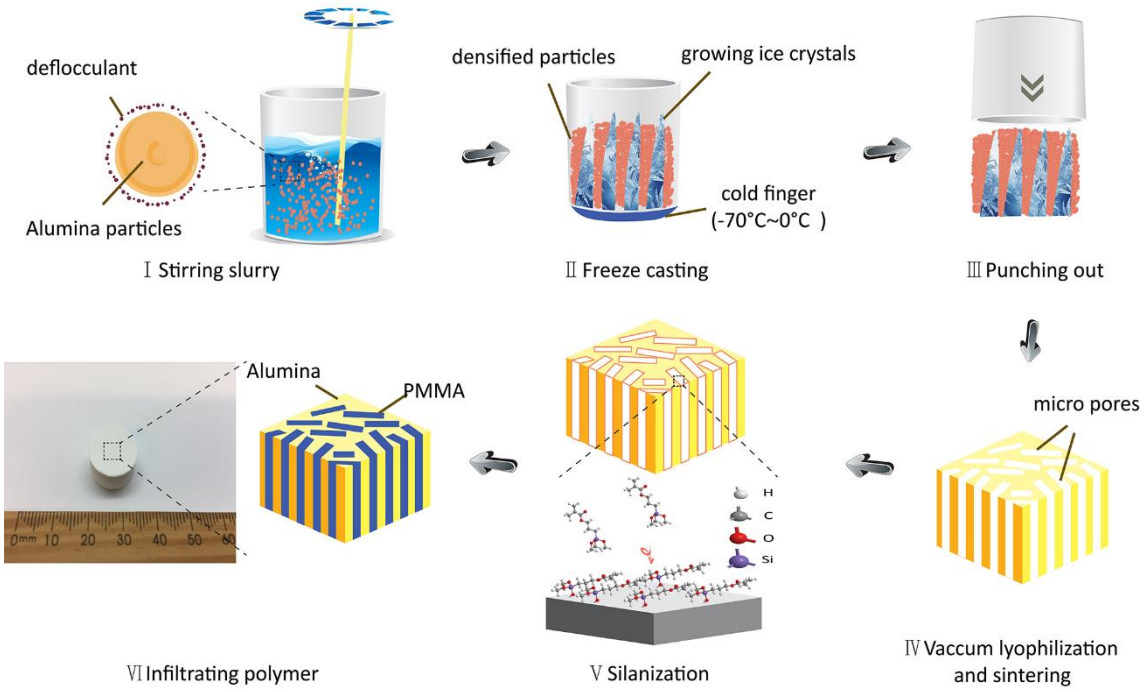

Figure 1

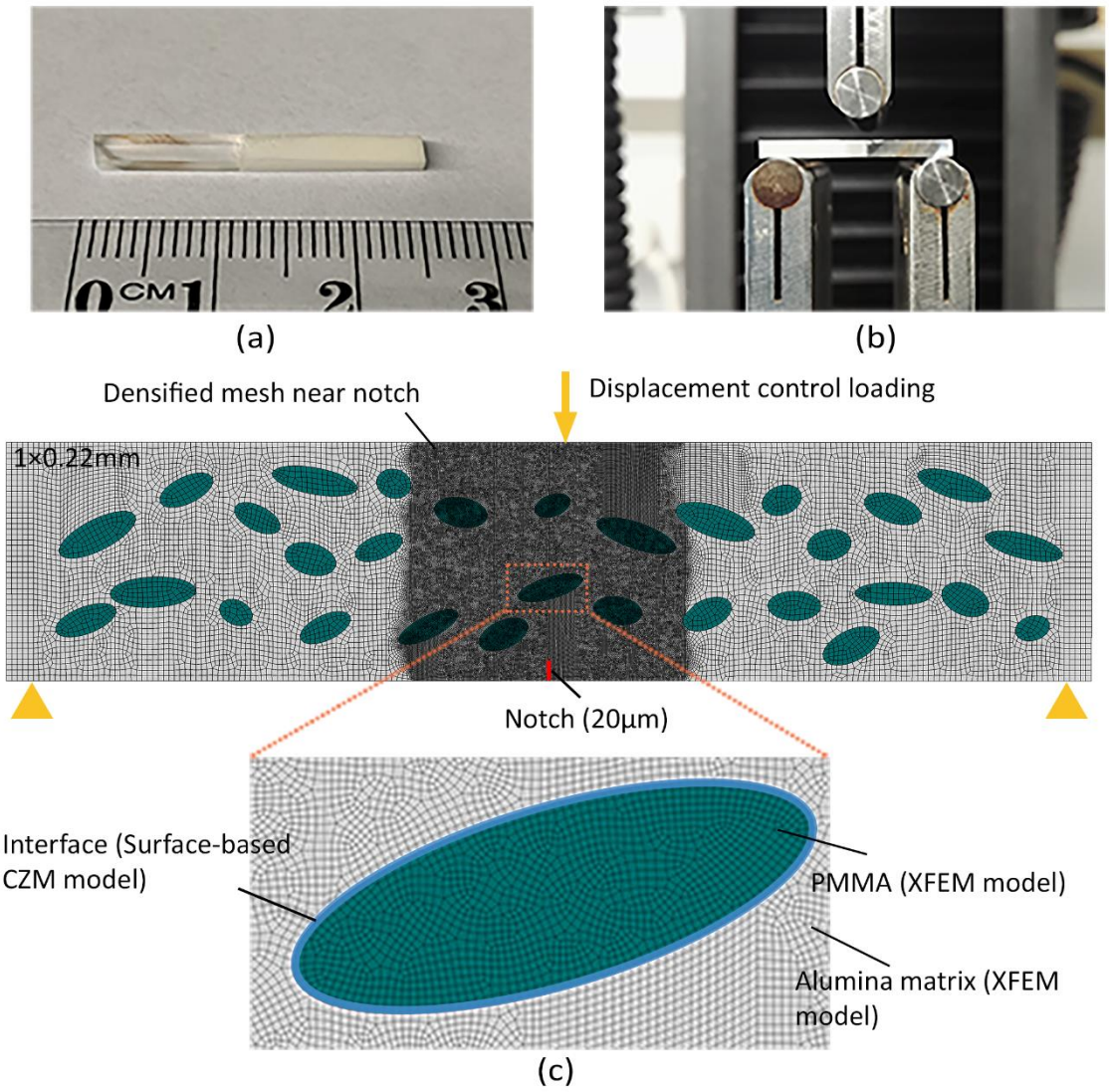
(a)
(b)
Densified mesh near notch
Displacement control loading
1×0.22mm
Notch (20μm)
Interface (Surface-based CZM model)
PMMA (XFEM model)
Alumina matrix (XFEM model)
(c)

Figure 2

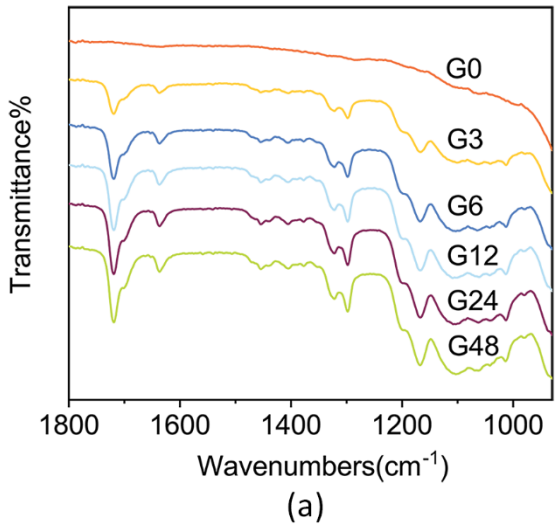
G0
G3
G6
G12
G24
G48
Transmittance%
1800
1600
1400
1200
1000
Wavenumbers(cm-1)

(a)

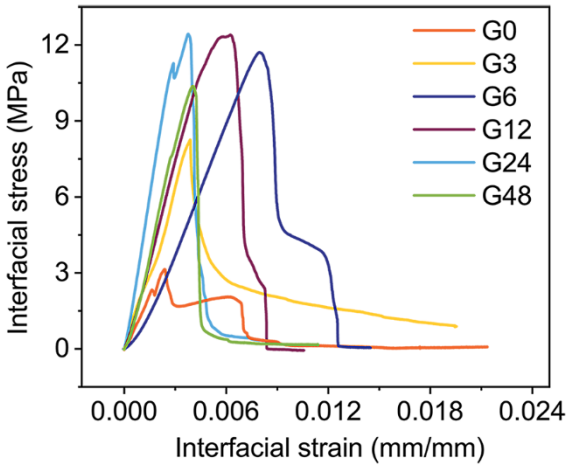
G0
G3
G6
G12
G24
G48
Interfacial stress (MPa)
12
9
6
3
0
0.000
0.006
0.012
0.018
0.024
Interfacial strain (mm/mm)

(b)

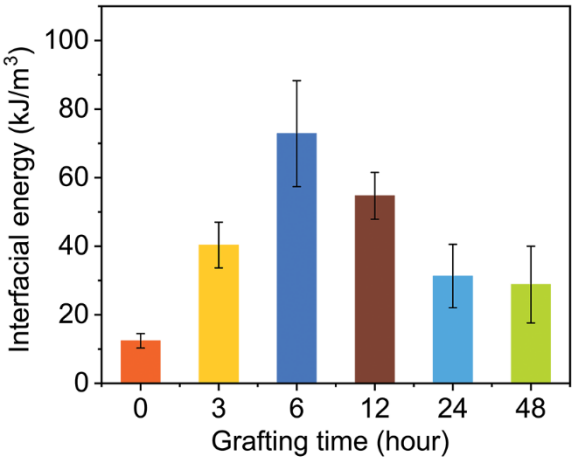
Interfacial energy (kJ/m3)
100
80
60
40
20
0
0
3
6
12
24
48
Grafting time (hour)

(c)

Figure 3

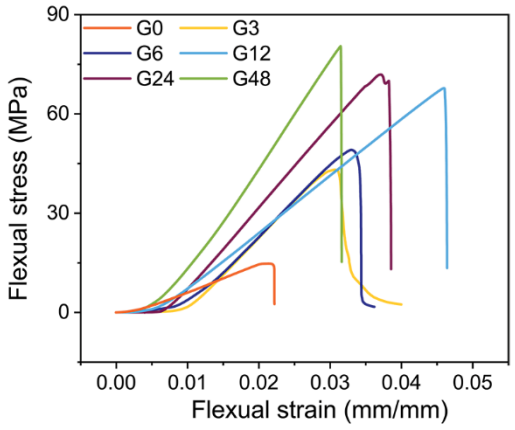
G0
G3
G6
G12
G24
G48
Flexual stress (MPa)
Flexual strain (mm/mm)
0
30
60
90
0.00
0.01
0.02
0.03
0.04
0.05

(a)

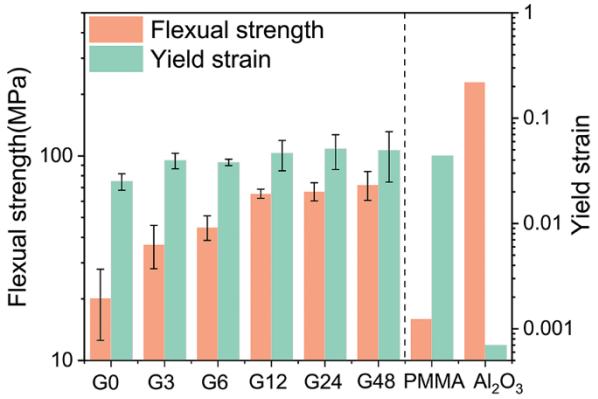
Flexual strength
Yield strain
Flexual strength(MPa)
Yield strain
10
100
0.001
0.01
0.1
1
G0
G3
G6
G12
G24
G48
PMMA
Al2O3

(b)

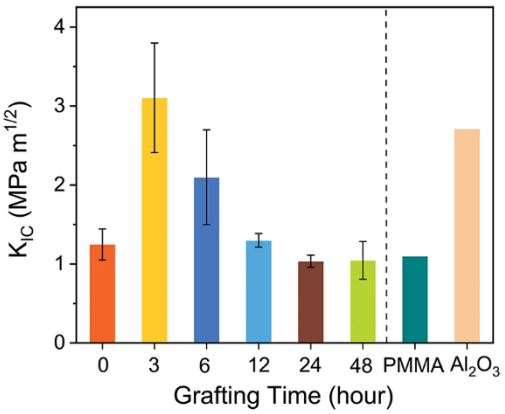
K_IC (MPa m^1/2)
0
1
2
3
4
0
3
6
12
24
48
PMMA
Al2O3
Grafting Time (hour)

(c)

Figure 4

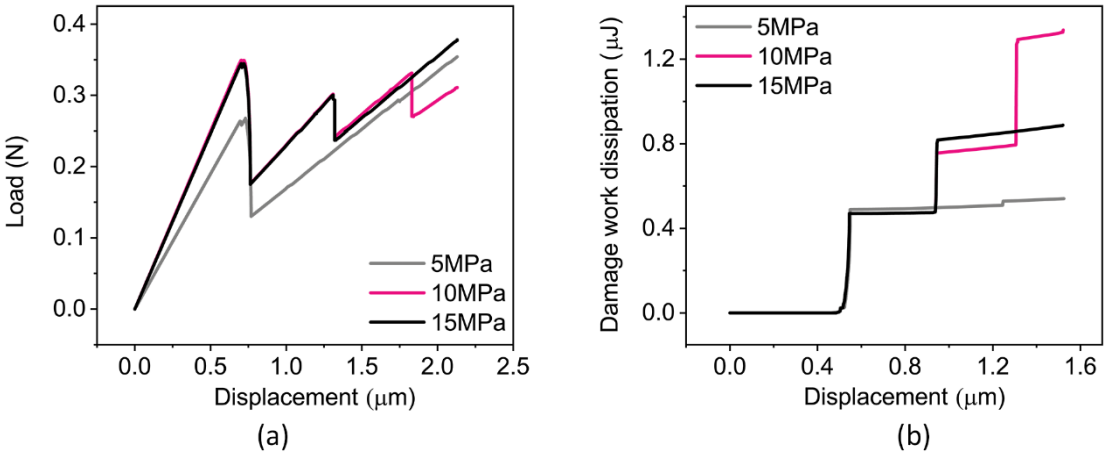
Load (N)
0.4
0.3
0.2
0.1
0.0
0.0
0.5
1.0
1.5
2.0
2.5
Displacement (μm)
5MPa
10MPa
15MPa
(a)
Damage work dissipation (μJ)
1.2
0.8
0.4
0.0
0.0
0.4
0.8
1.2
1.6
Displacement (μm)
5MPa
10MPa
15MPa
(b)

Figure 5

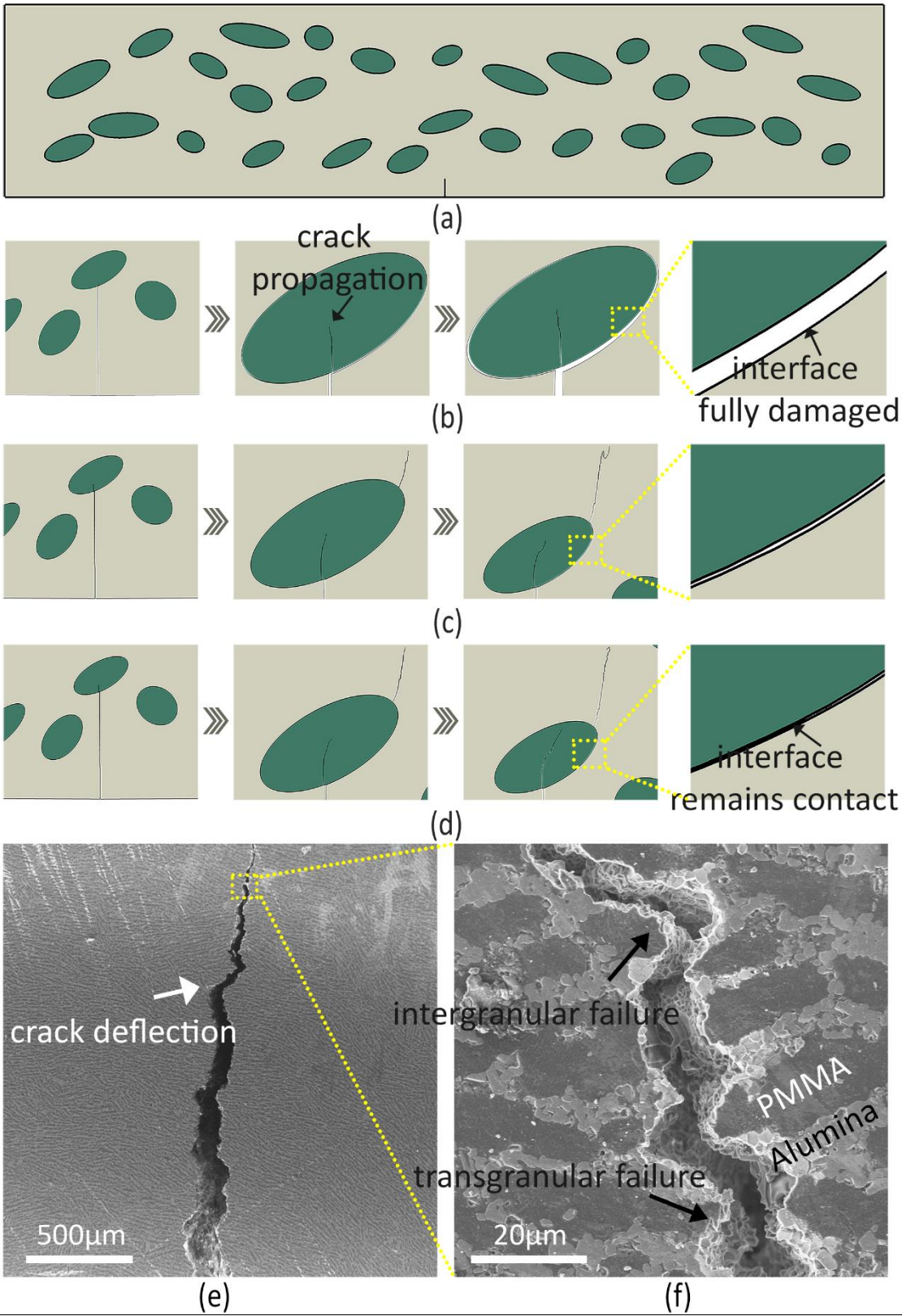
(a)
crack
propagation
interface
fully damaged
(b)
(c)
interface
remains contact
(d)
crack deflection
intergranular failure
PMMA
Alumina
transgranular failure
500μm
20μm
(e)
(f)

Figure 6

Table 1 structural properties of freeze casting samples

	Pore dimensions (µm)		Porosity (%)	Density (g/cm^3)	shrinkage (%)
	Pore space (d)	**Lamella thickness (t)**			
1 % dispersant	5±2	6±3	71.9±0.2	1.11±0.01	89.3±0.3
4 % dispersant	12±8	7±3	65.4±1.4	1.36±0.06	83.4±1.1
8 % dispersant	10±9	8±3	75.4±0.7	0.97±0.03	93.4±0.9